Journal of Crystal Growth 311 (2008) 47–53

Contents lists available at ScienceDirect

Journal of Crystal Growth

journal homepage: www.elsevier.com/locate/jcrysgro

Strained GaSb/AlAsSb quantum wells for p-channel field-effect transistors

Brian R. Bennett *, Mario G. Ancona, J. Brad Boos, Corwyn B. Canedy, Saara A. Khan

Electronics Science and Technology Division, Naval Research Laboratory, 4555 Overlook Avenue, SW, Washington, DC 20375-5347, USA

ARTICLE INFO

Article history:
Received 21 August 2008
Received in revised form
23 September 2008
Accepted 11 October 2008
Communicated by H. Asahi
Available online 18 October 2008

PACS:
72.80.Ey
73.61.Ey
81.05.Ea
85.30.Tv

Keywords:
A3. Molecular beam epitaxy
A3. Quantum wells
B2. Semiconducting III–V materials
B2. Semiconducting gallium compounds
B2. Semiconducting ternary compounds
B3. Field effect transistors

ABSTRACT

Quantum wells of GaSb were grown by molecular beam epitaxy on GaAs substrates. The buffer layer and barrier layers consisted of relaxed $AlAs_xSb_{1-x}$. The composition of the $AlAs_xSb_{1-x}$ was varied to produce compressive biaxial strains in the GaSb. The confinement and strain in the GaSb quantum wells lift the degeneracy in the valence band, resulting in lower in-plane effective mass and higher mobility. A three-fold enhancement of mobility was achieved, with room-temperature mobilities as high as 1350 $cm^2/V\,s$ and 77 K values as high as 10,400 $cm^2/V\,s$ for strains near 1%. These quantum wells should be suitable for high-performance p-channel field-effect transistors for complementary circuits operating at extremely low power.

Published by Elsevier B.V.

1. Introduction

Over 20 years ago, the first high-electron-mobility transistors (HEMTs) were reported. Since then, both GaAs- and InP-based HEMTs have exhibited excellent high-frequency performance. In recent years, several groups have also reported progress in InAs- and InSb-channel HEMTs [1]. Because of their small bandgaps and high electron mobilities, these semiconductors offer high-speed performance at much lower power. For example, antimonide-based HEMT low-noise amplifiers using InAs channels operate at frequencies of 10–100 GHz. They consume 3–10 times less power than comparable InP- or GaAs-based circuits [1]. In addition, a two-stage S-band amplifier with a total power dissipation of only 365 μW was demonstrated [2]. Recently, there has been interest in the potential of III–V field-effect transistors (FETs) for advanced logic applications, which could enhance digital circuit functionality and extend Moore's law [3]. For these applications, a key to low-power operation is the ability to make complementary circuits. In III–V materials, one challenge centers on maximizing the hole mobility in p-channel FETs [4].

The use of strain to reduce hole effective masses by splitting the heavy-hole (HH) and light-hole (LH) valence bands was proposed and demonstrated in p-channel InGaAs/(Al)GaAs quantum wells [4–7]. More recently, the technique has been applied to strained Ge layers on lattice-relaxed SiGe buffer layers, with room-temperature mobilities greater than 3000 $cm^2/V\,s$ [8,9]. For this work, we employ a similar strategy with the goal of demonstrating a narrow-bandgap channel material with relatively high hole mobility. Recently, we examined InGaSb as a channel material [10,11]. In the present work, we investigate GaSb as the channel material, with a potential advantage being the absence of alloy scattering in the channel.

2. Experimental procedure

In the case of $In_xGa_{1-x}Sb$ quantum wells on an AlGaSb buffer layer, the level of compressive strain in the quantum well was controlled by changing channel composition [10]. In contrast, in this work we changed the buffer layer composition in order to control the strain in the GaSb quantum well. The heterostructures studied here are grown by molecular beam epitaxy (MBE) on semi-insulating GaAs using a Riber Compact 21T system. The $AlAs_xSb_{1-x}$ buffer/barrier material is grown as a digital superlattice by

*Corresponding author. Tel.: +1 202 767 3665; fax: +1 202 767 1165.
E-mail address: brian.bennett@nrl.navy.mil (B.R. Bennett).

0022-0248/$ - see front matter Published by Elsevier B.V.
doi:10.1016/j.jcrysgro.2008.10.025

toggling the As and Sb shutters while the Al shutter and the As and Sb valves remain open [12,13]. The AlAs mole fraction can be adjusted by changing the length of time the As shutter is open relative to the Sb shutter.

In Fig. 1, we show the cross section for most of the samples in this study. Following oxide desorption, a 0.1 μm layer of GaAs is grown near 580 °C. Then, the temperature is lowered to 525 °C and a 0.1 μm layer of AlSb is grown, followed by 0.8–2.6 μm of the $AlAs_xSb_{1-x}$ digital alloy. This is followed by a 4.5 nm $AlAs_xSb_{1-x}$(Be) modulation-doping layer, a 10.5 nm $AlAs_xSb_{1-x}$ spacer, and a 7.5–12.5 nm GaSb quantum well. The final layers consist of a 10.5 nm $AlAs_xSb_{1-x}$ barrier, a 4 nm $In_{0.2}Al_{0.8}Sb$ etch-stop layer, and a 2 nm InAs cap. The $AlAs_xSb_{1-x}$ composition is varied between samples, but remains constant within each sample. The GaSb channel and InAs cap layers were grown at a rate of 0.2 monolayers (ML)/s; all other layers were grown at 0.7–1.2 ML/s. Valved crackers were used for As and Sb, with cracking zone temperatures of 950 °C, yielding As_2 and a mixture of Sb_2 and Sb_1. The substrate temperature was measured by transmission spectroscopy [14]. For some samples, the substrate temperature was reduced prior to the growth of the GaSb well and subsequent layers. In Fig. 2, we show a calculated band structure for an $AlAs_{0.25}Sb_{0.75}$/GaSb structure. Note that the band alignment is well suited for confinement of holes in the GaSb, with a valence band offset near 0.6 eV.

The $AlAs_xSb_{1-x}$ buffer layer is almost fully relaxed and accommodates the ~7% lattice mismatch with the GaAs substrate.

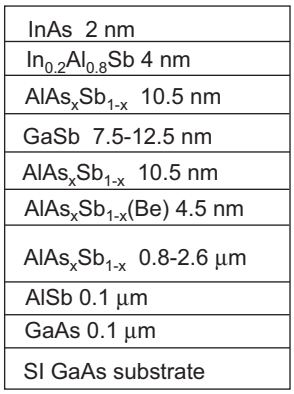

Fig. 1. Cross-section of typical GaSb/AlAsSb quantum-well heterostructure. The $AlAs_xSb_{1-x}$ layers are composed of AlSb/AlAs short-period superlattices.

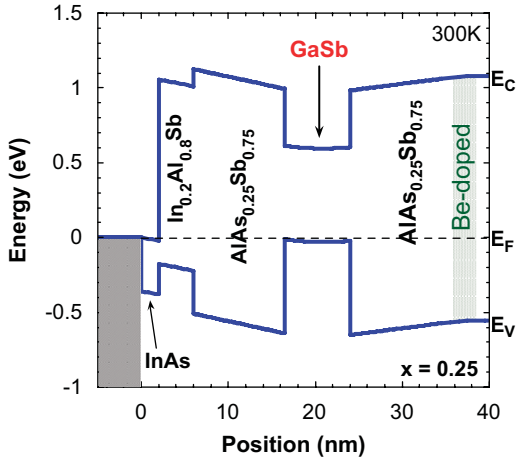

Fig. 2. Calculated band-structure for a GaSb/$AlAs_{0.25}Sb_{0.75}$ quantum well.

The GaSb channel is in biaxial compression. For a buffer layer of $AlAs_xSb_{1-x}$, the in-plane pseudomorphic strain associated with the lattice mismatch between the GaSb channel and buffer layer is given by

$$\varepsilon = (x - 0.08469)/(12.958 - x) \quad (1)$$

The heterostructures were characterized with X-ray diffraction measurements made on a double-crystal system using Cu-K_α radiation, and compared with simulations using dynamical diffraction theory. Hall–van der Pauw transport measurements were made on $5 \times 5\,mm^2$ squares at 300 and 77 K, using fields of 0.37, 0.55, and 1.0 T. Before cleaving samples for transport measurements, 55-point resistivity maps were generated using a Lehighton 1500 contactless microwave system [15].

Some samples were rotated throughout the growth of the buffer layers and active layers. Based upon previous results on this MBE system, we expect the layer thicknesses to be uniform to within 1% across the 76-mm-diameter wafers. For other samples, however, we intentionally did not rotate during the $AlAs_xSb_{1-x}$ buffer layer. This resulted in AlAs mole fractions which varied by nearly a factor of two across the wafer. A few $5 \times 5\,mm^2$ squares were cleaved from different locations on the wafer. Each of these small pieces was characterized by X-ray diffraction and transport, thereby providing an efficient means of obtaining multiple samples from a single epitaxial growth. Samples with a number after the letter (e.g., T1, T2, T3, and T4) were from a single epitaxial growth with a nonuniform buffer layer.

In Fig. 3 results are plotted of 6×6 k.p calculations, performed using the nextnano device simulation program (see www.nextnano.de) for the in-plane dispersion of a 7.5 nm quantum well of GaSb clad by $AlAs_{0.21}Sb_{0.79}$. The figure shows the highest energy HH and LH bands. The degeneracy at k=0 is lifted by the 1% compressive strain in the GaSb and quantum confinement, with the HH1 band highest in energy and hence with greater occupancy. This splitting is expected to lead to higher mobility both because the in-plane mass of the HH band is lower and because of the reduced density of final states for scattering.

In Fig. 4, we show the calculated occupancies for the various valence bands as a function of strain for a 7.5 nm GaSb quantum well with a sheet density of $1 \times 10^{12}/cm^2$. For the unstrained case,

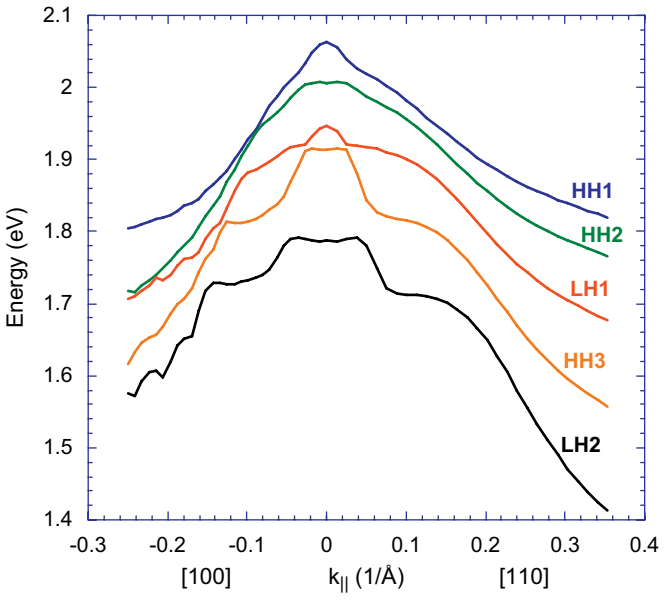

Fig. 3. Calculated dispersion curves for holes in a 7.5 nm GaSb/$AlAs_{0.21}Sb_{0.79}$ quantum well. The GaSb is under 1% compressive strain.

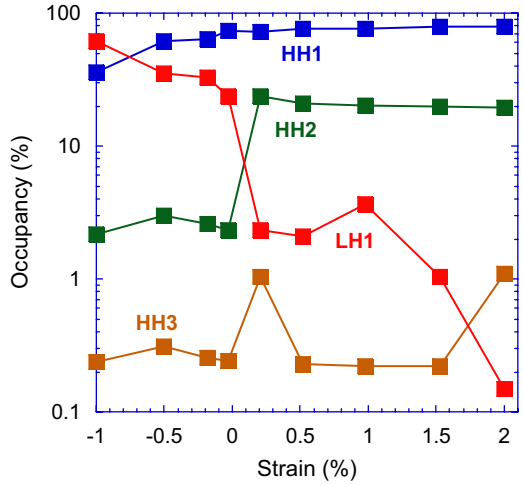

Fig. 4. Calculated occupancy of hole bands as a function of strain in 7.5 nm GaSb quantum wells with a hole density of $1\times10^{12}/cm^2$. Compressive strains are positive; tensile strains are negative.

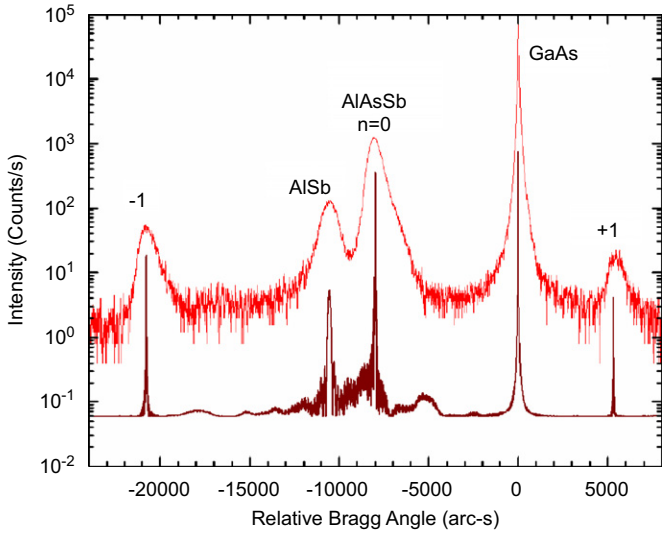

Fig. 5. Double-crystal X-ray diffraction data for sample L (upper curve) and simulation (lower curve). AlSb and AlAs thicknesses in the buffer layer short-period superlattice were varied to obtain a good fit to the experimental data.

the degeneracy is lifted by quantum confinement, and the occupancy of the HH1 band is 73%, compared to 24% for the LH1 band. For samples in compression, about 80% of the holes reside in the HH1 band, with most of the remainder in the HH2 band. In contrast, where there is sufficient tensile strain the occupation of the LH1 band becomes dominant. In general, significant occupation of a second sub-band degrades mobility due to the higher density of final states. In addition, if the highest sub-band has a larger in-plane effective mass, as in the case of the LH1 band (note smaller curvature in Fig. 3), then additional degradation in mobility is expected. From these considerations, we expect channel materials in compression to yield the highest mobilities.

3. Results and discussion

In Fig. 5, we show the X-ray scan for sample L which has the structure shown in Fig. 1 with an AlAsSb buffer thickness of 1.0 μm and a GaSb thickness of 10 nm. The buffer layer consisted of 666 periods of 3.9 s AlSb/1.1 s AlAs. Peaks are visible for the GaAs substrate, the 100 nm AlSb buffer layer, and the digital superlattice (n=−1, 0, and +1). A simulation using superlattices with 1.083 nm AlSb and 0.337 nm AlAs is also shown. The period of 1.42 nm is in reasonable agreement with the nominal value of 1.51 nm derived from reflection high-energy electron diffraction oscillations. The relaxation for the superlattice was assumed to be 100%. The relaxation for the 100 nm AlSb layer was treated as a free parameter; a value of 98% yields a good match to the peak position, as shown in Fig. 5. The epilayer peaks are all broadened compared to the simulation. This is a result of a high density of misfit dislocations required to relax the ~7% lattice mismatch. Using the superlattice layer thicknesses and Vegard's law, we calculate the effective ternary composition to be $AlAs_{0.238}Sb_{0.762}$. Using Eq. (1), the compressive biaxial strain in the GaSb is 1.21%. The X-ray full-width at half-maximum for the n=0 superlattice peak is 690 arcsec. Table 1 includes the alloy composition, quantum-well thickness and strain, superlattice period, buffer layer thickness, growth conditions, and transport results for all samples with uniform (rotated) buffer layers. Table 2 contains the same information for samples with nonuniform (not rotated) buffer layers.

The ability to control the $AlAs_xSb_{1-x}$ alloy composition and hence the GaSb quantum-well strain is essential for this work. Using short-period superlattices, we achieved good reproducibility and control of the alloy composition. As an example, in Fig. 6 we show the alloy composition of four samples grown within a 20-day period. (The base temperatures of the Sb- and As-valved cracking cells were not adjusted during this period.) To increase the AlAs mole fraction, we increased the As duty cycle in increments of 0.1 s, decreasing the Sb duty cycle by the same amount. As the duty cycle of the As is increased, the AlAs mole fraction increases. The SL period remains relatively constant as expected.

The density of electrons or holes in the channel is important for FET technologies. In our work, the thicknesses of the doped and spacer layers were fixed, and the Be flux was varied. For samples A and K, no dopants were used and the hole sheet density was $6–8\times10^{11}/cm^2$. In Fig. 7, we plot the sheet density of holes as a function of the Be dopant cell temperature. The solid line was calculated by using the activation energy (3.21 eV) measured for thick layers of GaAs(Be), accounting for the background ($7\times10^{11}/cm^2$), and matching one of the 843 °C data points. It is clear that we have good control over the sheet density in the range of $1–3\times10^{12}/cm^2$; this range encompasses most n- and p-channel FETs.

For rotated samples, the nonuniformity (defined as the standard deviation divided by the mean) of resistivity over a 76 mm wafer was 2–5%, suggesting that both the mobility and density are relatively uniform. For example, the resistivity map for sample L is shown in Fig. 8a. In contrast, samples grown without rotation during the buffer layer exhibit large changes in resistivity, as shown in Fig. 8b for sample P. The resistivity varies from 4300 to 9900 Ω/sq as a result of the change in the $AlAs_xSb_{1-x}$ alloy composition, the GaSb strain, and the GaSb mobility across the sample.

As shown in Tables 1 and 2, several structural/growth parameters were varied in an attempt to optimize the room-temperature mobility and sheet resistance. These include AlAs mole fraction in the buffer layer, and equivalently strain in quantum well, buffer layer thickness, quantum-well thickness, and quantum-well growth temperature. Samples Q and R were grown on the same day, with only the quantum-well thickness varying (10 and 15 nm, respectively). The samples were not rotated during growth of the AlAsSb buffer layers, yielding

Table 1
Summary of growth conditions and materials parameters for all samples grown with substrate rotation during the buffer layer.

Name	As (%)	Strain (%)	t_{Buff} (μm)	SL-period (nm)	t_{QW} (nm)	T_{QW} (°C)	T_{Be} (°C)	n_{300} ($\times 10^{12}$/cm^2)	μ_{300} (cm^2/V s)	n_{77} ($\times 10^{12}$/cm^2)	μ_{77} (cm^2/V s)
K	0.0	−0.53	1.1	–	10	500	–	0.6	580	1.0	2000
M	8.2	−0.021	1.1	3.67	10	450	822	1.1	430	1.5	3560
N	10.1	0.13	1.1	3.55	30	450	822	1.1	680	1.1	6130
A	17.7	0.72	1.1	2.09	7.5	500	–	0.8	730	1.1	6040
B	18.6	0.79	1.1	1.72	7.5	500	865	2.6	780	2.8	4660
H	19.3	0.96	0.9	1.40	10	450	822	1.2	690	1.5	2500
E	22.0	1.06	1.1	1.45	7.5	500	843	1.4	1080	1.6	6190
D	22.4	1.09	1.1	1.47	7.5	500	843	1.4	1050	1.6	6330
L	23.8	1.21	1.0	1.42	10	450	822	1.2	1000	1.5	4320
C	24.1	1.23	1.0	1.37	7.5	500	843	1.6	1020	2.1	4790
G	27.2	1.48	1.1	1.45	7.5	500	843	1.7	670	1.9	1890
I	29.3	1.64	0.9	1.40	10	450	843	1.6	680	1.5	1320
F	31.0	1.78	1.0	1.42	12.5	500	843	1.7	790	2.1	2150
J	31.4	1.81	0.9	1.40	10	500	843	1.5	560	1.3	990

Values of As fraction in the $AlAs_xSb_{1-x}$, GaSb quantum-well strain (positive for compressive and negative for tensile), buffer layer thickness, superlattice period, quantum-well thickness and growth temperature, Be cell temperature, and hole density and mobility at 300 and 77 K are included.

Table 2
Summary of growth conditions and materials parameters for all samples grown without substrate rotation during the buffer layer.

Name	As (%)	Strain (%)	t_{Buff} (μm)	SL-period (nm)	t_{QW} (nm)	T_{QW} (°C)	T_{Be} (°C)	n_{300} ($\times 10^{12}$/cm^2)	μ_{300} (cm^2/V s)	n_{77} ($\times 10^{12}$/cm^2)	μ_{77} (cm^2/V s)
P1	18.8	0.81	1.3	1.81	10	400	822	1.2	1180	1.6	6150
P2	37.5	2.31	0.8	1.01	10	400	822	1.3	340	1.1	340
Q1	19.1	0.83	2.6	1.88	10	400	822	1.4	1180	1.3	8000
Q2	19.3	0.85	2.5	1.81	10	400	822	1.1	1350	1.3	8460
Q3	24.0	1.22	2.1	1.50	10	400	822	1.4	950	1.2	2990
Q4	34.9	2.09	1.6	1.16	10	400	822	1.1	430	–	–
R1	33.7	2.00	1.6	1.13	15	400	822	1.2	230	0.8	100
R2	24.0	1.22	2.0	1.44	15	400	822	2.2	510	–	–
R3	19.6	0.87	2.5	1.78	15	400	822	1.5	830	1.2	4700
S1	18.6	0.79	1.5	1.77	10	470	822	1.2	920	1.2	7100
S3	23.2	1.16	1.1	1.29	10	470	822	1.5	870	1.4	2630
S4	36.3	2.21	1.2	1.35	10	470	822	1.5	410	1.3	560
S5	21.6	1.03	1.4	1.62	10	470	822	1.2	1120	1.3	6600
T1	18.1	0.75	1.4	1.68	10	470	822	1.1	1060	1.2	10400
T2	20.9	0.97	1.4	1.58	10	470	822	1.2	1170	1.2	8980
T3	23.0	1.14	1.2	1.37	10	470	822	1.2	1040	1.3	4360
T4	33.4	1.97	0.9	1.02	10	470	822	1.4	410	1.5	990
U1	18.1	0.76	1.4	1.60	10	440	855	2.1	810	2.5	2610
U2	24.4	1.25	1.1	1.19	10	440	855	1.8	840	2.1	2820
V1	–	−0.93	–	–	10	440	822	0.4	410	–	–
V2	–	−1.02	–	–	10	440	822	0.1	310	–	–

Values of As fraction in the $AlAs_xSb_{1-x}$, GaSb quantum-well strain (positive for compressive and negative for tensile), buffer layer thickness, superlattice period, quantum-well thickness and growth temperature, Be cell temperature, and hole density and mobility at 300 and 77 K are included.

nonuniformity in the strain across the wafer. We measured 3–4 pieces from each wafer. The room-temperature mobility is plotted as a function of buffer layer composition in Fig. 9. Across the range of strains, the 10 nm quantum well has higher mobilities than its 15 nm counterpart. Presumably, the thicker well exceeds a critical layer thickness over the entire range of strain, resulting in relaxation of strain via misfit dislocations in the quantum well. In addition, the wider well will have less splitting due to the confinement which could produce lower mobilities. For quantum-well thicknesses between 7.5 and 12.5 nm, the mobility was not a strong function of well thickness (see Table 1).

As we will discuss in detail, most of the parameters that we varied did not have a major impact on mobility over the range investigated. The parameter that had the largest impact was quantum-well strain. In Fig. 10, we plot the room-temperature mobility as a function of quantum-well strain for samples with quantum-well thickness varying from 7.5 to 12.5 nm. [Sample R, 15 nm (discussed above) and sample N, 30 nm, are not included.] The upper axis shows the AlAs mole fraction in the quantum well. Most of our work focused on samples with compressive strain in the GaSb quantum well. As expected, there is a strain-induced enhancement of mobility, with 11 samples exceeding 1000 cm^2/V s. Sample K was grown with an AlGaSb buffer layer (no As). The quantum well was in tensile strain (−0.53%) and the mobility was 580 cm^2/V s. To obtain an unstrained quantum well, we grew sample M with an $AlAs_{0.082}Sb_{0.918}$ buffer layer. The superlattice growth times were 12.0 s for AlSb and 1.0 s for AlAs, yielding 33.7 Å AlSb and 3.0 Å AlAs per period. The mobility was 430 cm^2/V s which is lower than most of the strained samples. Presumably, the absence of strain-induced splitting of the valence bands resulted in a lower mobility for M. Sample N was nominally the same as M but with a 30 nm quantum well. For nearly lattice-matched samples, the critical layer thickness is large. A thicker quantum well with less interface scattering could result in an enhancement of mobility. The room-temperature mobility of sample N is indeed higher, 680 cm^2/V s. As shown in Table 1, the 77 K mobility increases from 3560 cm^2/V s for M to 6130 cm^2/V s for N.

To investigate larger tensile strains, we grew sample V with an $In_yAl_{1-y}Sb$ buffer layer. The GaSb quantum well was 10 nm thick.

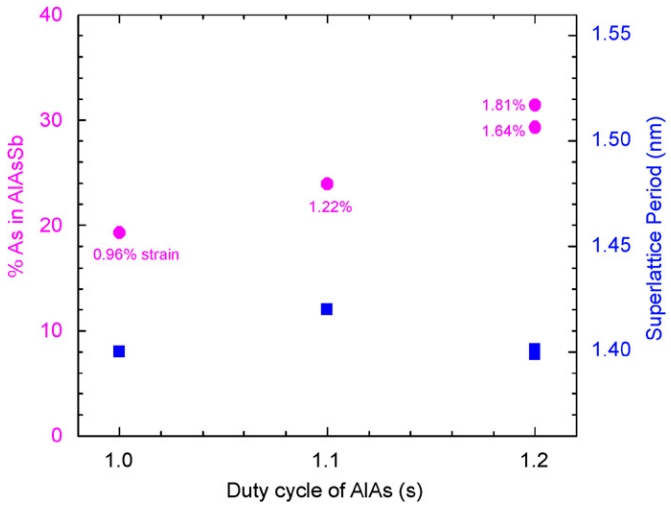

Fig. 6. Buffer layer composition (●) and superlattice period (■) as a function of AlAs duty cycle for samples grown within a 20-day period. Total growth time per period is fixed at 5.0 s.

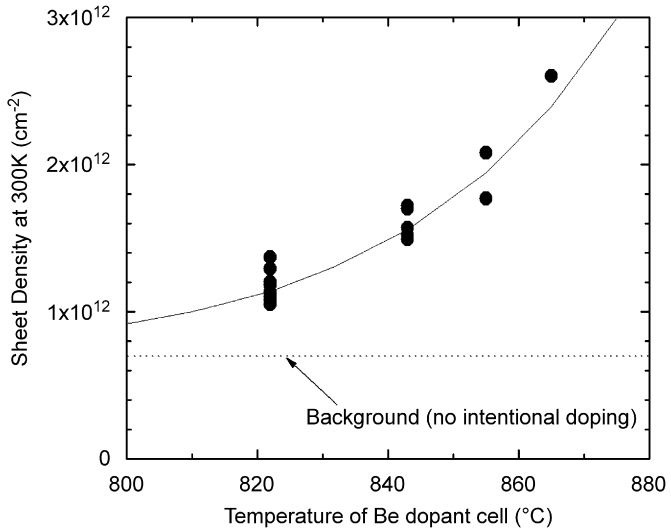

Fig. 7. Hole sheet density as a function of Be dopant cell temperature. The solid line is calculated (see text).

The sample was not rotated during the buffer layer. Two $5 \times 5\,mm^2$ samples, V1 and V2 were characterized. The InSb mole fractions, *y*, were 0.049 and 0.065, yielding GaSb tensile strains of 0.93% and 1.02%, respectively. As shown in Table 2, the room-temperature mobilities were 410 and 310, respectively. These results are qualitatively consistent with the calculations in Fig. 4 that suggested tensile strain will be much less effective than compressive strain for mobility enhancement. It is also possible that the lower mobilities are a result of a smaller critical layer thickness for tension than compression or a lower quality for the InAlSb buffer layer compared to the AlAsSb layers used for compressively-strained GaSb quantum wells.

Previous reports of p-doped GaSb quantum wells used Al(Ga)Sb buffer layers, resulting in quantum wells with ~0.5% tensile strain. As shown in Fig. 10, the room-temperature mobilities were 180–280 $cm^2/V\,s$ [16–18], compared to sample K with a mobility of 580 $cm^2/V\,s$. The densities for the samples from the literature ranged from $1.8–5.0 \times 10^{12}/cm^2$. If the higher densities resulted in occupation of additional sub-bands, this could account for the lower mobilities. We note, however, that

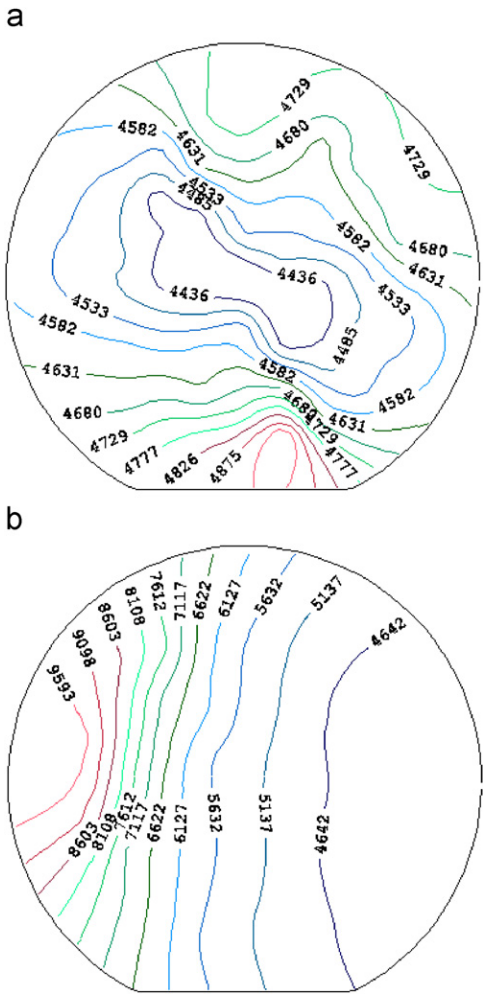

Fig. 8. Resistivity maps in units of Ω/sq for (a) sample L, rotated during buffer layer, and (b) sample P, not rotated during buffer layer. The large variation in (b) is a result of varying strain in the GaSb quantum well.

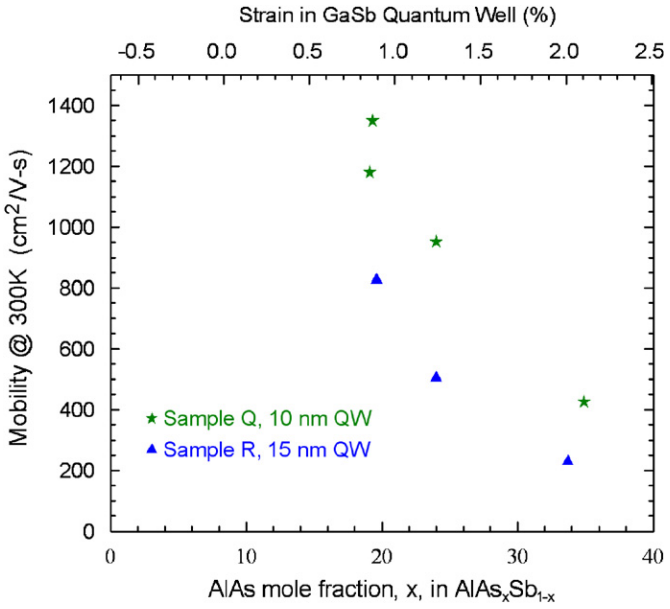

Fig. 9. Room-temperature mobility as a function of buffer layer composition (or GaSb quantum-well strain) for two samples grown the same day, differing only in quantum-well thickness.

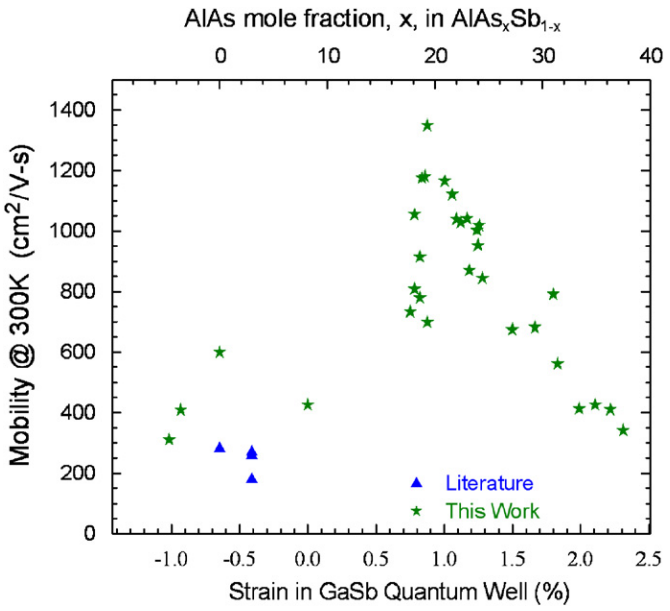

Fig. 10. Room-temperature mobility as a function of GaSb quantum-well strain (or buffer layer composition) for all samples with quantum-well thickness between 7.5 and 12.5 nm. Data from the literature for GaSb/AlGaSb quantum wells is also included [16–18]. The highest mobilities are achieved for quantum-well strains near 1%.

samples A and B in our study were similar except that B was doped, yielding $2.6\times10^{12}/cm^2$ at 300 K compared to $0.8\times10^{12}/cm^2$ for A. They have similar mobilities, suggesting that mobility is not a strong function of density in this range. Sample B has a sheet resistivity of 3100 Ω/sq, the lowest of any sample in this study.

Room-temperature transport properties were measured at fields of 0.37, 0.55, and 1.0 T, with at least two currents for each B-field for all samples. The six measurements generally gave results that varied by 1–10%. Measurements at 77 K were made at 0.37 and 0.55 T, with two currents at each field. The results often differed by 10–30%. The 300 and 77 K values included in Tables 1 and 2 were chosen to be representative of the measured values. We note that sample K (discussed above) has a mobility of 2000 cm^2/V s at 77 K, a value comparable to values in the literature for GaSb/AlGaSb quantum wells with similar strains [16–18]. There is some correlation between the 300 and 77 K mobilities; all samples with a 300 K mobility above 1000 cm^2/V s have a 77 K mobility greater than 4000 cm^2/V s. The highest 77 K mobility was 10,400 cm^2/V s for sample T1. We note that the highest 77 K mobility achieved for InGaSb/AlGaSb quantum wells was also about 10,000 cm^2/V s [10].

Higher growth temperatures generally result in fewer point defects. In the case of strained layers, higher growth temperatures can result in more kinetically-limited lattice relaxation. In this work, the quantum well growth temperature was varied from 400 to 500 °C. As shown in Tables 1 and 2, room-temperature mobilities in excess of 1000 cm^2/V s were achieved throughout this range, suggesting that the transport characteristics are relatively insensitive to growth temperature over this range.

Most of our samples included an annealing step to produce a flat surface before deposition of the quantum well. After growth of the AlAsSb spacer layer, the samples were ramped to 550 °C under an Sb flux and held there for 111 s before cooling and GaSb quantum-well growth. Samples S and T were grown on the same day. The only nominal difference was that the annealing step was omitted for sample T. As shown in Table 2, the mobilities were comparable for these samples across a range of strains, suggesting the annealing step was neither beneficial nor harmful.

AlAs, AlSb, and alloys of $AlAs_xSb_{1-x}$ are highly reactive in air, making it difficult to achieve a stable mesa floor during a typical FET isolation process [19]. To mitigate this problem, we grew three structures, samples H, I, and J, in which 20% of the Al was replaced by Ga. As seen in Table 1 and Fig. 10, they have room-temperature mobilities that are comparable to samples with similar strains but without Ga in the buffer layer.

The AlAsSb buffer layer is expected to contain a high density of misfit dislocations, which relieve the 7% strain. Studies of GaSb buffer layers on GaAs indicate a rapid reduction in the dislocation density as the thickness increases [20]. Similar behavior may be expected for AlAsSb buffer layers with comparable lattice mismatches. As a result, thicker buffer layers may result in higher quality quantum wells. As shown in Tables 1 and 2, buffer layer thicknesses ranged from 0.8 to 2.6 μm in this study. There is no clear correlation between buffer layer thickness and room-temperature mobility with mobilities greater than 1000 cm^2/V s obtained for buffer layers ranging from 1.0 to 2.6 μm.

The highest room-temperature mobility was 1350 cm^2/V s for sample Q2 with a strain of 0.85%. Mobilities dropped below 1000 cm^2/V s for compressive strains greater than 1.2%, presumably due to the relaxation of strain via misfit dislocations in the quantum well. A similar trend was observed for $In_zGa_{1-z}Sb$ quantum wells on AlGaSb buffer layers, but in that case the highest mobilities (~1500 cm^2/V s) were reached near 2% strain [10]. It is not clear why dislocations apparently form at a lower strain in the GaSb quantum wells compared to InGaSb. One possibility is that the AlAsSb buffer layers provide a larger source of threading dislocations than the AlGaSb buffer layers [21]. If that is the case, then a substantial reduction in the dislocation density from the use of a graded buffer layer of AlAsSb could allow larger strains in the GaSb quantum well and higher mobilities.

4. Summary

In summary, we have grown and characterized p-channel GaSb quantum-well heterostructures. Compressive strain, induced by a lattice mismatch between the GaSb and an $AlAs_xSb_{1-x}$ buffer layer, modifies the band structure, resulting in higher hole mobilities, with room-temperature mobilities as high as 1350 cm^2/V s. These structures should be suitable as p-channel FETs and are an important step toward the goal of high-performance complementary circuits operating at extremely low power.

Acknowledgments

The authors thank C.L. Canedy, N.A. Papanicolaou, and B.V. Shanabrook for technical discussions. This work was partially supported by the Office of Naval Research.

References

[1] B.R. Bennett, R. Magno, J.B. Boos, W. Kruppa, M.G. Ancona, Solid State Electron. 49 (2005) 1875.
[2] W. Kruppa, J.B. Boos, B.R. Bennett, N.A. Papanicolaou, D. Park, R. Bass, Electron. Lett. 42 (2006) 688.
[3] R. Chau, S. Datta, M. Doczy, B. Doyle, J. Jin, J. Kavalieros, A. Majumdar, M. Metz, M. Radosavljevic, IEEE Trans. Nanotechnol. 4 (2005) 153.
[4] P.P. Ruden, M. Shur, D.K. Arch, R.R. Daniels, D.E. Grider, T.E. Nohava, IEEE Trans. Electron Devices 36 (1989) 2371.
[5] G.C. Osbourn, Superlattices Microstruct. 1 (1985) 223.
[6] M. Jaffe, J.E. Oh, J. Pamulapati, J. Singh, P. Bhattacharya, Appl. Phys. Lett. 54 (1989) 2345.
[7] T.J. Drummond, T.E. Zipperian, I.J. Fritz, J.E. Schirber, T.A. Plut, Appl. Phys. Lett. 49 (1986) 461.

[8] M.L. Lee, E.A. Fitzgerald, M.T. Bulsara, M.T. Currie, A. Lochtefeld, J. Appl. Phys. 97 (2005) 011101.
[9] M. Myronov, K. Sawano, Y. Shiraki, T. Mouri, K.M. Itoh, Appl. Phys. Lett. 91 (2007) 082108.
[10] B.R. Bennett, M.G. Ancona, J. Brad Boos, B.V. Shanabrook, Appl. Phys. Lett. 91 (2007) 042104.
[11] J.B. Boos, B.R. Bennett, N.A. Papanicolaou, M.G. Ancona, J.G. Champlain, R. Bass, B.V. Shanabrook, Electron. Lett. 43 (2007) 834.
[12] Y.H. Zhang, J. Crystal Growth 150 (1995) 838.
[13] C.L. Canedy, G.I. Boishin, W.W. Bewley, C.S. Kim, I. Vurgaftman, M. Kim, J.R. Lindle, J.R. Meyer, L.J. Whitman, J. Vac. Sci. Technol. B 22 (2004) 1575.
[14] B.V. Shanabrook, J.R. Waterman, J.L. Davis, R.J. Wagner, Appl. Phys. Lett. 61 (1992) 2338.
[15] M. Passlack, R. Droopad, K. Rajagopalan, J. Abrokwah, R. Gregory, D. Nguyen, IEEE Electron Device Lett. 26 (2005) 713.
[16] J.F. Klem, J.A. Lott, J.E. Schirber, S.R. Kurtz, S.Y. Lin, J. Electron. Mater. 22 (1993) 315.
[17] L.F. Luo, K.F. Longenbach, W.I. Wang, IEEE Electron Device Lett. 11 (1990) 567.
[18] K. Yoh, H. Taniguchi, K. Kiyomi, M. Inoue, Jpn. J. Appl. Phys. 1 (30) (1991) 3833.
[19] S. Miya, S. Muramatsu, N. Kuze, K. Nagase, T. Iwabuchi, A. Ichii, M. Ozaki, I. Shibasaki, J. Electron. Mater. 25 (1996) 415.
[20] R.N. Kutt, R. Scholz, S.S. Ruvimov, T.S. Argunova, A.A. Budza, S.V. Ivanov, P.S. Kopyev, L.M. Sorokin, M.P. Shcheglov, Fiz Tverd Tela+ 35 (1993) 724.
[21] B.R. Bennett, Appl. Phys. Lett. 73 (1998) 3736.